Cellulose (2017) 24:4627–4639
DOI 10.1007/s10570-017-1453-0

ORIGINAL PAPER

Toughening mechanisms in cellulose nanopaper: the contribution of amorphous regions

Rui Mao · Nan Meng · Wei Tu · Ton Peijs

Received: 11 February 2017 / Accepted: 12 August 2017 / Published online: 30 August 2017

Abstract Cellulose nanopaper is a strong and tough fibrous network composed of hydrogen bonded cellulose nanofibres. Upon loading, cellulose nanopaper exhibits a long inelastic portion of the stress–strain curve which imparts high toughness into the material. Toughening mechanisms in cellulose nanopaper have been studied in the past but mechanisms proposed were often rather speculative. In this paper, we aim to study potential toughening mechanisms in a systematic manner at multiple hierarchical levels in cellulose nanopaper. It was proposed that the toughness of cellulose nanopaper is not, as is often assumed, entirely caused by large scale inter-fibre slippage and reorientation of cellulose nanofibres. Here it is suggested that dominant toughening mechanism in cellulose nanopaper is associated with segmental motion of molecules facilitated by the breakage of hydrogen bonds within amorphous regions .

R. Mao · N. Meng · T. Peijs (✉)
School of Engineering and Materials Science, Queen Mary University of London, Mile End Road, London E1 4NS, UK
e-mail: t.peijs@qmul.ac.uk

W. Tu
Nanoforce Technology Ltd., Joseph Priestley Building, Queen Mary University of London, Mile End Road, London E1 4NS, UK

Keywords Nanocellulose · Nanopaper · Yielding · Plasticity · Toughness

Introduction

Cellulose widely exists in plant cell walls in the form of microfibrils (Barnett and Bonham 2004; Keckes et al. 2003). The repeat unit in the cellulose molecule consists of two anhydroglucose rings which are linked by β-1,4 glycosidic bonding (Klemm et al. 1998). Cellulose nanofibres can be extracted in the form of individual microfibrils and/or their aggregations by deconstructing the cell wall structure (Eichhorn et al. 2010). Cellulose nanofibre is composed of crystalline regions where cellulose chains are believed to align parallel to the axis of the nanofibre together with amorphous regions where cellulose chains are not-ordered (Haslach 2000). Crystalline regions are separated by amorphous regions at intervals of up to 800 Å, with individual cellulose molecules connecting several crystalline and amorphous regions (Haslach 2000; Salmén 1986). The amorphous cellulose is also present at the surface of the crystallites. Cellulose crystals prepared via acid hydrolysis displayed a crystallinity index of about 80% (Kargarzadeh et al. 2012), which suggests a contribution of cellulose chains within the crystallite surface to the amorphous phase of the nanofibres. Cellulose nanopaper is a fibrous network composed of cellulose

nanofibres connected together by van der Waals forces and hydrogen bonding. Because of improved mechanical properties of nanofibres over micro-sized cellulose fibres, in combination with an increased network density, it shows superior mechanical properties compared with conventional paper. Tensile strengths and Young's moduli of cellulose nanopaper have been reported to be around 200 MPa and 13 GPa, respectively (Henriksson et al. 2008). Its strain-to-failure can reach a value as high as 10%, imparting high toughness into the cellulose nanopaper (work to fracture = 15.1 MJ m^{-3}) (Henriksson et al. 2008). Typical stress–strain curves of cellulose nanopaper show an elastic region followed by a long inelastic region where the toughness primarily originates from. Therefore, the exploration of toughening mechanisms in cellulose nanopaper should focus on mechanisms of inelasticity in such nanopapers.

So far, many papers have focused on the structure–property relation of cellulose nanopaper, while the reported mechanisms are all rather speculative. Hsieh et al. (2008) proposed that the inelastic portion in the stress–strain curve is related to breakdown of the fibrous network by bond breaking and fibre pull-out. They also proposed that twisting of individual cellulose fibrils could possibly contribute to inelasticity. Henriksson et al. (2008) prepared cellulose nanopapers with different porosities by drying cellulose nanopapers from solvents of various polarities. They speculated that inelasticity is related to inter-fibrillar debonding and slippage of nanofibrils promoted by voids. Sehaqui et al. (2011) reported that higher porosity and higher surface area led to weaker inter-fibre bonds, resulting in a lower tensile modulus and higher strain-at-break of nanopapers and a weaker strain hardening behaviour in the inelastic region of the stress–strain curve. The dependence of yield stress on the degree of polymerization of the cellulose molecules and length of the nanofibres was also investigated but no clear trend was observed (Fukuzumi et al. 2013; Henriksson et al. 2008). The inelastic behaviour can be changed by changing humidity (Benitez et al. 2013). It was reported that inelasticity is facilitated by high humidity, and it was proposed that here inelasticity is caused by inter-fibrillar debonding and possible sliding. Inter-fibrillar hydrogen bonds can be weakened and broken by water molecules, leading to breakage of hydrogen bonds and reduced inter-fibrillar friction (Benitez et al. 2013; Quero et al. 2011). Robust cellulose nanopapers have been produced by hot pressing, with inelastic behaviour being more pronounced for less well pressed nanopapers (Österberg et al. 2013). It was speculated that nanopapers that were hot pressed for longer periods of time were denser and had fewer voids. By this more hydrogen bonds could form after extended periods of high pressure and temperature. The effect of microvoids on the mechanical properties of all-cellulose fibreboard was also reported by Arévalo and Peijs (2016) where denser fibreboard resulted in higher mechanical properties. Recently, Zhu et al. (2015) proposed that the high toughness of cellulose nanopaper was caused by breaking and reformation of hydrogen bonding during inter-fibre slippage. The hypothesis was supported by results of atomistic simulation. Structure–property relationships of cellulose nanopaper were also studied using finite element modelling of fibrous networks (Mao et al. 2017). From literatures it can be concluded that the inelasticity of cellulose nanopaper is generally speculated to be associated with the break-down of hydrogen bonds between cellulose nanofibres together with inter-fibre slippage. However, so far no direct evidence exists for such a hypothesis.

Cellulose nanofibres are composed of macromolecules, which are organized in crystalline and amorphous domains or regions. Therefore there is a distinct possibility that the non-linear behaviour in these materials is related to the same phenomena that promote inelastic behaviour in semi-crystalline polymers. This paper will therefore focus on mechanisms for inelasticity in cellulose nanopaper at different length scales. First, a two-dimensional digital image correlation (2D DIC) technique, which has been used earlier to characterize the strain distribution in paperboard by Hagman and Nygårds (2012) was applied to cellulose nanopaper. Next, the possibility of inter-fibre slippage between individual cellulose nanofibres and subsequent reorientation of nanofibres during the inelastic stage was examined using repeated loading–unloading experiments, in situ Raman spectroscopy and wide angle X-ray diffraction (WAXD). Finally, the relationship between local mobility of molecular chain segments in amorphous domains and inelastic behaviour was investigated using polarized optical microscopy (POM), tensile testing performed at different strain rates and temperatures, as well as temperature dependent dielectric spectroscopy.

Materials and methods

Materials

Preparation of cellulose nanofibres

Nanofibrillated cellulose (NFC) nanofibres were kindly provided by Prof. Berglund's group at KTH Stockholm (Sweden). The NFC was prepared from softwood pulp provided by Nordic Pulp and Paper (Sweden). The lignin and hemicellulose contents were 0.7 and 13.8%, respectively. Following Henriksson et al. (2007), the pulp was dispersed in deionized water followed by a pretreatment process involving a combination of an enzymatic treatment (Novozym 476, Novozymes A/S, Denmark) and mechanical beating in a laboratory beater (PFI mill, Hamjern Maskin, Norway). This pretreated pulp was homogenized by 8 passes through a microfluidizer (M-110EH, Microfluidics Inc., USA). From this a water suspension with a solid concentration of 1.7% NFC was obtained.

Preparation of cellulose nanopaper

Cellulose nanopaper was prepared by first mixing NFC suspension with 0.2 g dry weight and approximately 40 mL distilled water. The speed of the mixer (IKA Ultra Turrax mixer D125 Basic, Germany) was 12,000 rpm and the mixing time was 10 min. Then the diluted suspension was degassed. Finally, the suspension was poured into a petri-dish followed by conditioning in an incubator at 37 °C for several days. During this time, silica-gel particles were also placed in the incubator in order to absorb the water vapour. The resulting cellulose nanopaper had a thickness of approximately 30 μm. The grammage and porosity of the cellulose nanopaper were 46 g m^{-2} and 11%, respectively. The porosity was calculated using Eq. 1.

$$Porosity = 1 - \frac{\rho_{nanopaper}}{\rho_{cellulose}} \quad (1)$$

where $\rho_{nanopaper}$ is the density of cellulose nanopaper and $\rho_{cellulose}$ is the density of cellulose which is 1500 kg m^{-3} (Henriksson et al. 2008).

Characterizations

Tensile testing

Tensile tests were conducted using universal testing machines (Instron 5566 and Instron 5584, USA). The load cell for all the tensile tests was 100 N. Specimens of 5 mm in width were used and conditioned at a temperature of 23 °C and a relative humidity (RH) of 50% for at least 24 h before testing. The distance between the clamps was 20 mm. First, tensile tests were performed at a speed of 2 mm min^{-1} using an Instron 5566 to obtain the stress–strain curve and mechanical properties of the nanopapers. Then, tensile tests were conducted at different strain rates and temperatures using an Instron 5584 equipped with an environmental chamber for temperature control. Environmental conditions during testing included: (1) a temperature of 23 °C and RH of 50% and (2) a temperature of 50 °C and RH of 50%, respectively. The results were based on at least six specimens for each sample. Strain was calculated using the cross-head displacement since the influence of frame compliance (<0.1%) can be neglected for the loads involved in these tests.

Repeated loading–unloading testing

Repeated loading–unloading experiments were performed on cellulose nanopaper to extract Young's modulus and yield stress for each cycle. The tests were carried out using an Instron 5566 universal testing machine (USA) equipped with a 100 N load cell. Specimen dimensions and conditioning (23 °C and 50% RH) were the same as in static tensile testing. The loading speed was 2 mm min^{-1}. The specimen was first loaded in the elastic region to obtain the elastic modulus. Then it was repeatedly loaded to different peak loads in the inelastic region where peak load was set to increase incrementally for each load cycle. The test was performed in triplicate to obtain averages.

2D Digital image correlation (2D DIC)

2D DIC technique was used to map the strain distribution in the tensile specimens. Specimen dimensions and conditioning were the same as in tensile testing. The surface of the specimens was first

spray coated with white paint to obtain a clear background (~6 μm in thickness). Then, black speckles of ~100 μm were sprayed on the surface of the specimen to achieve good contrast. The specimens were loaded in a micro-tensile tester (Deben, UK) equipped with a 200 N load cell. Distance between the clamps was 10 mm and the test speed was set at 0.2 mm min^{-1}. Images were taken by a CCD camera during loading. The pixel size for each picture was 9.0 μm × 9.0 μm. Displacement between speckles during loading was analysed by Ncorr, a Matlab programme developed at Georgia Institute of Technology, USA (Blaber et al. 2015).

Wide angle X-ray diffraction (WAXD)

Crystallinity of cellulose nanofibres forming cellulose nanopaper was determined from one-dimensional wide-angle X-ray diffraction (1D WAXD) patterns in a 2θ range of 5°–70°. The patterns were obtained using a Bragg–Brentano geometry X-ray diffractometer (X'Pert Pro, PANalytical, The Netherlands) equipped with Cu/Kα radiation. The obtained spectra were composed of sharp peaks from crystallites and broad background scattering from amorphous regions. Crystallinity of cellulose nanofibres forming cellulose nanopaper was calculated using Eq. 2 where the crystalline ($\sum A_c$) and amorphous fractions ($\sum A_a$) were obtained by fitting the spectra into 4 crystalline peaks and a broad band at approximately 21.5° which was assigned to amorphous contributions according to Park et al. (2010). The peak fitting was performed using PeakFit software (www.systat.com).

$$\chi_c = \frac{\sum A_c}{\sum A_c + \sum A_a} \times 100\% \quad (2)$$

The crystalline preferred orientation of cellulose nanofibres was examined using two-dimensional wide-angle X-ray diffraction (2D WAXD) ring patterns, which were obtained using a transmission geometry on a single crystal X-ray diffractometer (Kappa ApexII Duo, Bruker AXS GmbH, Germany). The measurements were carried out with the direction of the X-ray beam perpendicular to the plane of nanopaper, resulting in patterns in the in-plane direction. The 2D WAXD measurement was conducted on specimens before straining and post-fracture. Before straining, the X-ray was diverted to the specimen surface, while for failed specimens the X-ray was diverted to an area close to the fracture site. The surface area covered by X-ray was approximately 0.00785 mm^2.

Polarized optical microscopy (POM)

POM was used to examine the degree of anisotropy of specimens before and after tensile testing. The examination of molecular anisotropy is based on the fact that a linearly polarized incident light beam travelling through a uniaxially oriented material is split into two orthogonally polarized rays (ordinary and extraordinary rays) with different phase velocities so that a phase difference (δ) can be identified between the rays emerging from the material (Bhupathi et al. 2010). If a light beam with intensity of I_0 is incident on an anisotropic material which is placed between two crossed polarizers, the transmitted light intensity I can be given by Eq. 3 (Born and Wolf 1999).

$$I = I_0 \sin 2\varphi \sin^2 \frac{\delta}{2} \quad (3)$$

where φ is the angle between the optical axis and the polarization axis of the polarizer. In our case, the optical axis was assumed to be along the straining direction. For an isotropic material, the optical image will be dark no matter which direction the specimen is oriented. For an anisotropic material, the minimum transmitted light intensity (dark) can be obtained when the straining direction is along the direction of the polarizers. Maximum intensity (bright) can be obtained when the angle between straining direction and the polarization direction of each polarizer is 45°.

In the POM measurements, specimen dimension and conditioning were the same as in tensile testing. A specimen was first placed between two crossed polarizers where the direction of tension was aligned with one polarization direction (0°). One image was taken at a magnification of 5×. Another image was also taken when the same specimen was placed at an angle of 45°. Then, the specimen was stretched until failure using an Instron 5566 (USA) equipped with a 100 N load cell at a crosshead speed of 2 mm min^{-1}. Images of the failed specimen were taken close to the location of fracture, with the specimen being placed at angles of 0° and 45° relative to the polarization axis, respectively. A schematic of the test configuration is shown in Fig. 1. Anisotropy was identified if a specimen placed at an angle of 45° showed a brighter image than at 0°.

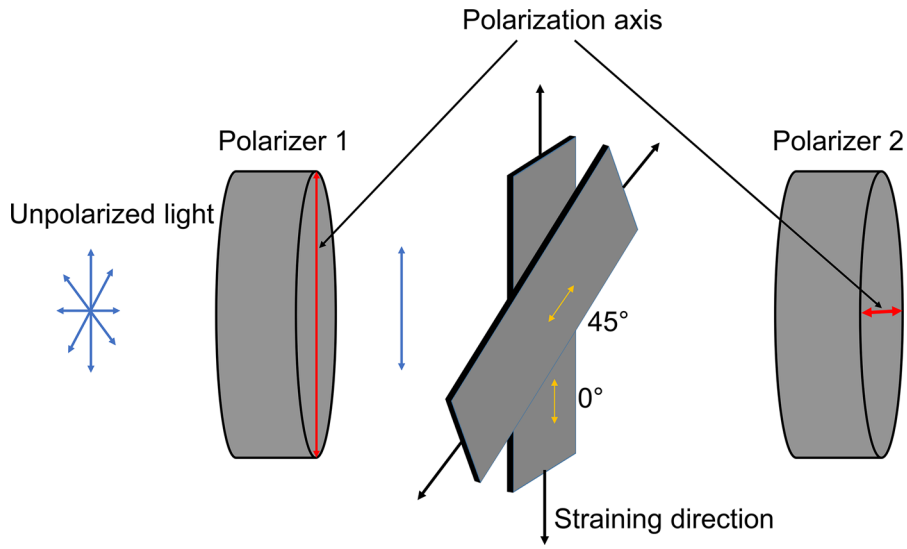

Fig. 1 Schematic of the experimental test setup for POM

In-situ Raman spectroscopy

The relationship between Raman band shifts and applied stresses and strains was investigated by recording Raman spectra using a Renishaw Raman Spectrometer (UK) equipped with a 633 nm Helium–Neon laser with a power of 35 mW during tensile testing. The laser power at specimen surface was 1–2 mW. The 1800 lines mm^{-1} diffraction grating was used and the resolution was 1 cm^{-1}. Specimen dimensions and conditioning were the same as in tensile testing. A specimen was mounted on a micro-tensile tester (Deben, UK) equipped with a 200 N load cell and loaded at a speed of 0.2 mm min^{-1}. The specimens were strained step-wise (0.2% strain increment), and at each step, the specimen was excited by a laser beam. A 50× objective lens was used to focus the laser beam on the surface of the specimen, while the spot size of the laser was ~2 µm. The wavenumbers used in the Raman spectra varied from 1050 and 1150 cm^{-1}. The Raman spectra were recorded using an exposure time of 10 s and three accumulations. The peak initially positioned at approximately 1095 cm^{-1} was determined by fitting the Raman band using a Lorentzian function. This test was triplicated.

Temperature dependent dielectric spectroscopy

The temperature dependence of the dielectric loss was measured using a LCR meter (4284A, Agilent Technologies, USA) connected to an in-house made oven. The measurements were conducted in a temperature range of −180 to 245 °C at four different frequencies, 100, 10 kHz, 1000 and 100 Hz.

Results and discussion

Figure 2 shows a stress–strain curve of cellulose nanopaper. The mechanical properties of the nanopaper are listed in Table 1. It can be seen that cellulose nanopaper deforms elastically until a strain of

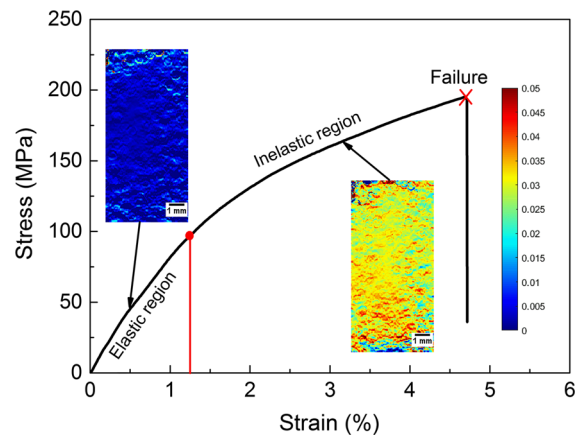

Fig. 2 Stress–strain curve of cellulose nanopaper. The *red line* sections the stress–strain curve into elastic and inelastic regions based on the 0.2% offset 'yield' point. The *insets* are 2D DIC strain distribution plots at different levels of strain (*scale bar* 1 mm). The degree of strain is indicated by the far *right bar* in the graph. (Color figure online)

Table 1 Mechanical properties of cellulose nanopaper

Young's modulus (GPa)	Strength (MPa)	Strain-to-failure (%)	Work to fracture (MJ m^{-3})
10.4 ± 0.9	196 ± 22	4.96 ± 0.26	6.5 ± 0.7

approximately 1%, after which a long inelastic region occurs until final failure. The strain distribution in the nanopaper as measured by 2D DIC at different loading stages are shown as insets. The strain distribution image in the elastic region shows a relatively uniform strain distribution in the nanopaper plane, while a less uniform strain distribution exists in the inelastic region. At the latter stage, some nanofibres are less loaded than others with strain values at every position in the nanopaper exceeding the value at the transition from elastic to inelastic region, indicating that inelasticity occurs throughout the whole cellulose nanopaper.

Repeated loading–unloading experiments were carried out to investigate the effect of inelastic loading history on Young's modulus and yield stress (Fig. 3a). Here, the words 'plastic deformation' and 'yield stress' are used only based on phenomenological interpretations since the mechanisms of inelastic deformation remain unclear. The development of Young's modulus with number of cycles is shown in Fig. 3b. The specimens were first strained in the elastic region (loading cycle 1 and 2) in order to obtain the initial Young's modulus. The Young's modulus at cycle 1 and 2 is 9.6 ± 0.7 GPa. Subsequent loading cycles were performed in the inelastic region and it is shown that the Young's modulus remains constant for all cycles. Furthermore, the values of Young's modulus are similar in both the elastic and inelastic regions. This result is consistent with the data reported by Henriksson et al. (2008) who measured the Young's modulus of cellulose nanopaper as a function of the number of loading–unloading cycles, and reported that the modulus during loading remained relatively unchanged with cycles. The values of yield stress of the cellulose nanopaper against loading cycles are plotted in Fig. 3c. Also yield stress is fairly independent of number of loading cycles and does not show any clear trend. The results of these repeated loading–unloading tests indicate that inelastic deformation has no apparent effect on Young's modulus and yield stress. Therefore, the occurrence of large scale nanofibre reorientation in the inelastic region is not very plausible as this would affect these properties.

Raman spectroscopy was used to examine the micromechanics of cellulose nanopaper in both the elastic and inelastic region. Figure 4a shows the Raman spectra of cellulose nanopaper at different levels of strain where a band initially at approximately 1095 cm^{-1} which corresponds to the C–O and C–C stretching mode in the cellulose backbone can be observed for an undeformed specimen (Gierlinger et al. 2006; Quero et al. 2010; Wiley and Atalla 1987). This Raman band shifted to lower wavenumber positions when the cellulose nanopaper was stretched. This shift can be ascribed to molecular straining of the cellulose molecule (Eichhorn et al. 2001a). The shift of the Raman peak positions are plotted against applied stress and strain in Fig. 4b, c, respectively with the data fitted by linear functions with high correlation. The drawn lines in Fig. 4b, c are lines with gradient values that correspond to the ones listed in the figures. This indicates that cellulose molecules are stressed proportionally with the applied stress and/or strain. As the Raman band shift reflects the extent of molecular straining, the band shift rate (slope of Raman band shift against stress) will change if the contribution of the applied stress to molecular deformation changes (Eichhorn et al. 2001b). Therefore, it can be concluded that no change in such contribution was detected by Raman spectra.

One can imagine that if the inelasticity is dominated by large scale inter-fibre slippage and reorientation, the contribution of the applied stress to molecular straining will change when inelasticity takes place since slippage and reorientation in fibre scale would cause massive unloading in molecular chains. However, Raman spectra show that such a change cannot be detected, meaning that inelasticity is not dominated by large scale inter-fibre slippage and reorientation. The origin of inelasticity is therefore likely to be related to processes at a lower hierarchical level. The Raman band shift rate in Tanpichai et al's (2012) paper was $-0.5\ cm^{-1}\ \%^{-1}$ where its absolute value is

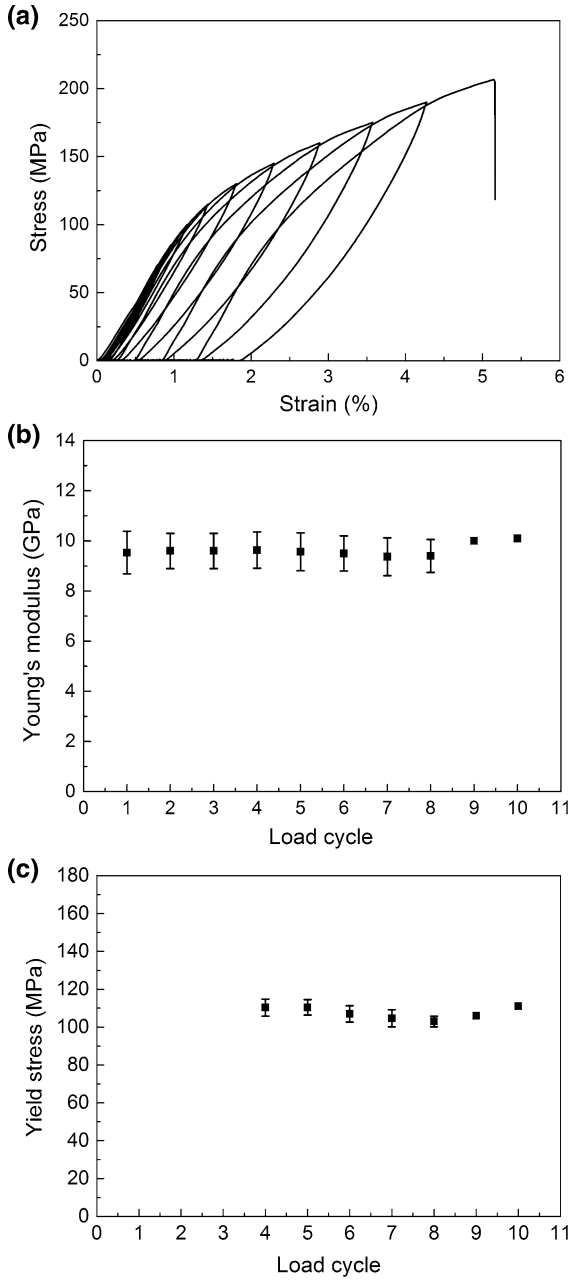

Fig. 3 **a** Repeated loading–unloading testing showing that the first two cycles are within the elastic region while subsequent cycles are in the inelastic region with incrementally increasing peak loads; **b** Young's modulus at each loading cycle and **c** yield stress at each loading cycle. The last two data points in **b**, **c** do not have *error bars* because two of the three measured specimens were broken after the 8th load cycle

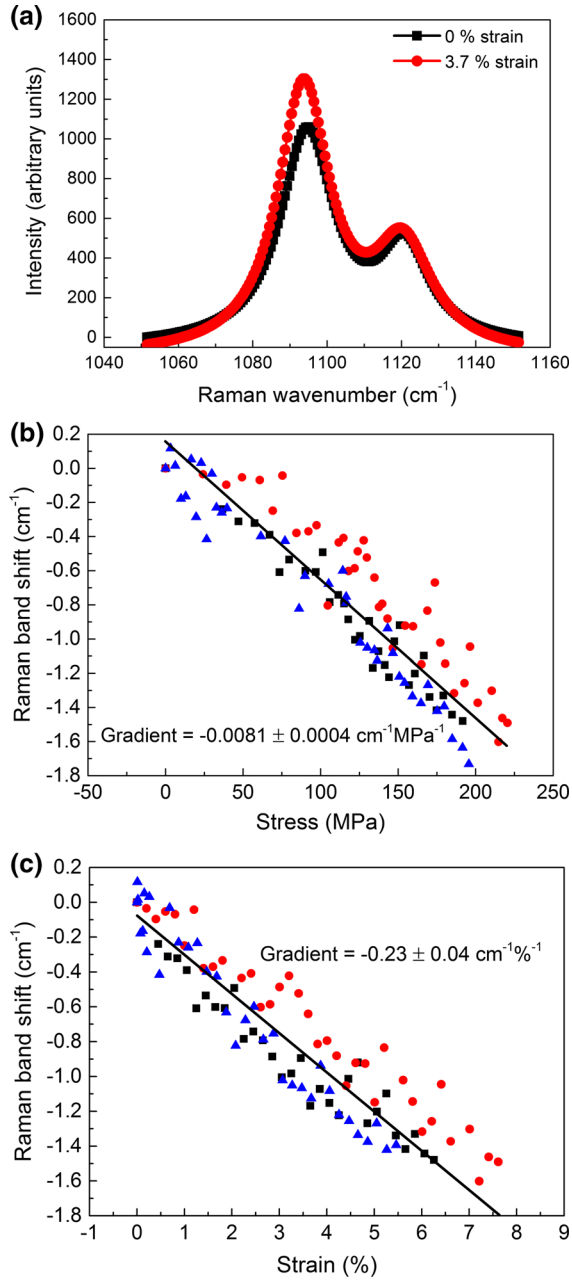

Fig. 4 **a** Raman band shift of 1095 cm^{-1} peak against strain, **b** the Raman band shift in the 1095 cm^{-1} as a function of stress and **c** the Raman band shift in the 1095 cm^{-1} as a function of strain. **b**, **c** the *dots* of different *shapes* and *colours* represent measurements performed on different nanopaper specimens. The gradients in **a**, **b** are average values of slopes obtained by linear fitting data from each specimen. The *drawn lines* in **b**, **c** are lines with gradient values that correspond to the ones listed in the figures

higher than the one measured in our current study ($-0.23\ cm^{-1}\ \%^{-1}$). Here, cellulose nanopaper was prepared through a suspension casting method where the resulting nanofibres are expected to be bend and the number of fibre–fibre bonds is relatively low. Tanpichai et al. prepared nanopapers by filtration of NFC suspensions followed by constrained drying of the filtered samples, resulting in straighter nanofibres and more inter-fibre bonds. Hence, the stress transfer ability in Tanpichai et al's nanopaper is expected to be better than in the nanopapers prepared by a suspension casting method, resulting in a stronger Raman band shift. In addition, the Raman band shift here cannot be used to calculate Young's modulus of cellulose nanopaper since the used Raman laser beam was not polarized. According to Tanpichai et al. (2012), a polarized laser beam is required to characterize the Young's modulus since the Raman band shift rate changes with the angle between polarization direction of the beam and strain direction. Therefore, our Raman band shift results can only be used for qualitative analysis.

In order to determine the crystallinity of the cellulose nanofibres in the nanopaper, the X-ray diffraction spectrum of cellulose nanopaper was analysed. Figure 5 shows the X-ray diffraction pattern of cellulose. It can be seen that the diffraction peaks are located at 2θ angles of 14.8°, 16.8°, 22.6°, 34.9°, which are typical native cellulose peaks (Tingaut et al. 2010). The calculated crystallinity is 68%, which means that cellulose nanopaper has amorphous

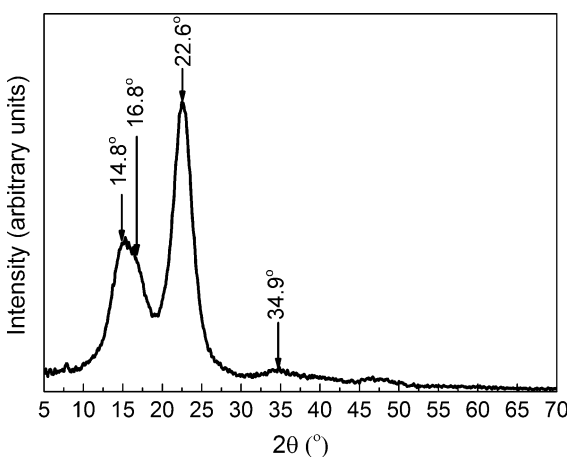

Fig. 5 X-ray diffraction spectra of cellulose nanopaper, showing typical native cellulose diffraction peaks located at 14.8°, 16.8°, 22.6°, 34.9°

domains or regions. Therefore, both the crystalline and amorphous phase need to be examined with respect to their contribution to the inelastic behaviour of cellulose nanopaper. Figure 5 also shows a reduced intensity for the cluster of reflections near the 004 peak at 34.9° on a Cu radiation pattern compared with the intensity for the reflections from randomly oriented crystallites, which indicates that crystallites in the cellulose nanopaper do show one-dimensional orientations (Segal et al. 1959; French and Cintrón 2013; French 2014).

Reorientation of nanofibers has been reported for specimens that were being drawn at a wet state prior to drying (Sehaqui et al. 2012). Here, the nanofibers reoriented because the hydrogen bonding was affected by the presence of water molecules which also acted as plasticizer between nanofibers. Therefore, nanofibers were able to move and align in the direction of an external force. Figure 6 shows the 2D WAXD data reflecting the in-plane degree of orientation. Tests were conducted on nanopapers before and after straining to failure (in a relative dry state). In-plane orientation of the crystallites in the paper is reasonably random before straining. Interestingly, this random orientation remained even when the specimen was stretched into the inelastic region and up to ultimate failure. The crystalline regions in the cellulose nanofibres did not reorient along the straining direction. This confirms our earlier hypothesis that cellulose nanofibres do not necessarily reorient in the inelastic region.

From above observations, it can be hypothesized that inelasticity in cellulose nanopaper is not the result of reorientation of cellulose nanofibres or crystalline regions in cellulose nanofibres. Hence, it is of interest to examine more closely the contribution of the amorphous regions in cellulose nanofibres to the inelastic deformation behaviour.

Figure 7 shows the images taken by POM with the nanopaper placed between crossed polarizers. Figure 7a, b show the optical images before straining, with the sample being positioned at the angles of 0° and 45° relative to the polarization axis, respectively. Images for both angles appear dark, indicating an isotropic structure of the cellulose nanopaper. Figure 7c, d show the optical images of samples after failure at angles of 0° and 45° relative to the polarization axis, respectively. The image at 0° is dark while the image at 45° appears bright. This

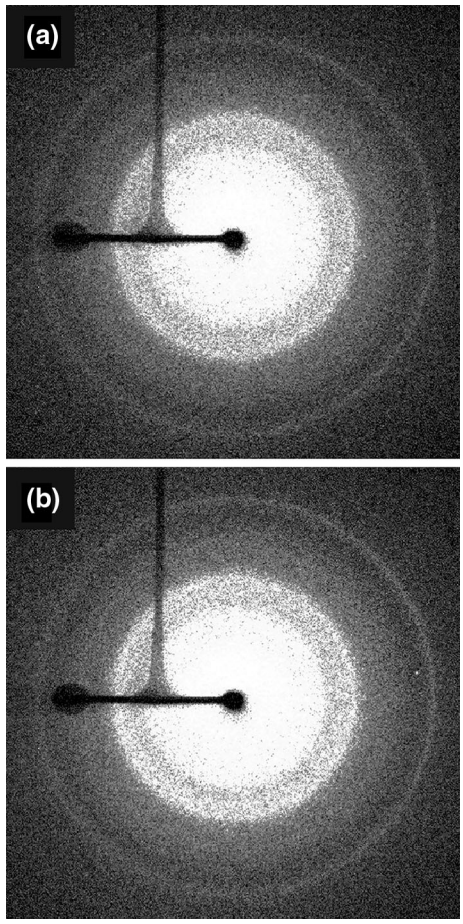

Fig. 6 2D WAXD patterns with the X-ray beam perpendicular to the cellulose nanopaper surface: **a** before straining, **b** after ultimate failure. No arcs can be observed in both images, which indicates the absence of preferential orientation

indicates that this sample exhibits some anisotropy upon straining in the inelastic region. Furthermore, it can be deduced that this anisotropy originates from amorphous regions.

Yielding in semi-crystalline or amorphous polymers such as polyethylene terephthalate (PET) (Lim et al. 2003), polycarbonate (PC) (Mulliken and Boyce 2006), poly(methyl methacrylate) (PMMA) (Mulliken and Boyce 2006), polypropylene (PP) (Alcock et al. 2007), poly(vinyl alcohol) (PVA) (Govaert and Peijs 1995) and plasticized starch blend (Chaléat et al. 2008) can be attributed to changes of chain conformation in amorphous regions, which depends on chain mobility. Yielding takes place when the molecular plastic strain rate resulting from chain mobility matches the applied strain rate. At high temperature, chain mobility increases so that molecular strain rate is easier to match applied strain rate resulting in a lower yield stress. Similarly, low strain rates result in a lowering of the yield stress (Engels et al. 2010; Kanters 2015; Mulliken and Boyce 2006; Van Erp et al. 2009). The relationship between yield stress and temperature and applied strain rate can be described by the Eyring equation (Chaléat et al. 2008; Senden et al. 2012; Söntjens et al. 2012).

$$\dot{\varepsilon} = \dot{\varepsilon}_0 \exp\left(-\frac{\Delta H}{RT}\right) \sinh\left(\frac{V\sigma_y}{RT}\right) \tag{4}$$

where $\dot{\varepsilon}$ is strain rate, σ_y is the yield stress, $\dot{\varepsilon}_0$ is the constant pre-exponential factor, ΔH is the activation energy, V is the activation volume, R is the gas constant and T is the absolute temperature. Equation 4 can be expressed as following

$$\frac{\sigma_y}{T} = \frac{R}{V} \sinh^{-1}\left(\frac{\dot{\varepsilon}}{\dot{\varepsilon}_0} \exp\left(\frac{\Delta H}{RT}\right)\right) \tag{5}$$

For large yield stress, Eq. 5 can reduce to

$$\frac{\sigma_y}{T} = \frac{R}{V}\left(\ln\left(\frac{2\dot{\varepsilon}}{\dot{\varepsilon}_0}\right) + \frac{\Delta H}{RT}\right) \tag{6}$$

Figure 8 shows the strain rate and temperature dependence of the yield stress for cellulose nanopaper. Temperature-normalized yield stress is plotted against the logarithmic strain rate for samples tested at different temperatures. In this paper, the 0.2% offset yield point is used since there is no maximum stress at yield point in the stress–strain curve. It can be seen that the normalized yield stress increases with strain rate but decreases with temperature. This indicates that lower strain rates and higher temperatures facilitate the mobility of cellulose molecules. Equation 6 was used to fit the data of the temperature-normalized yield stress versus logarithmic strain rate at different temperatures. It can be seen that the normalized yield stress increases linearly with the logarithm of strain rate, which indicates that one thermally activated process can be used to describe the yield behaviour under these conditions. The values of the activation parameters, ΔH and V, are shown in Fig. 8. The activation volume is 0.8 nm^3, which is defined as the product of cross-sectional area of the moving unit and its moving distance (Lim et al. 2003). This activation volume is of the order of activation volume values for polymers where molecular processes dominate

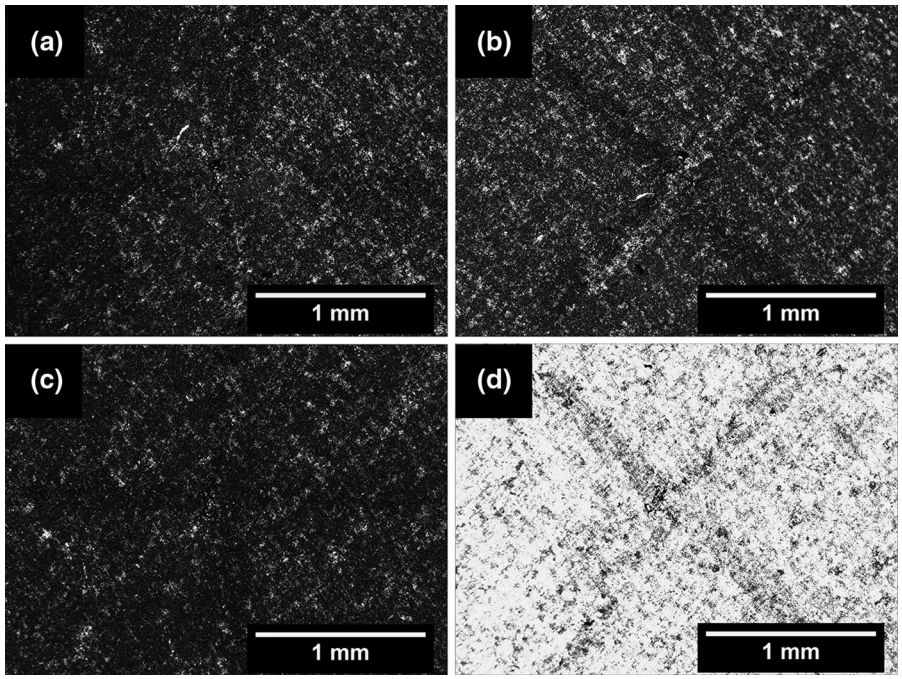

Fig. 7 POM images of cellulose nanopaper at different angles between straining direction and polarization direction: **a** before straining, 0° angle; **b** before straining, 45° angle; **c** after ultimate failure, 0° angle and **d** after ultimate failure, 45° angle. The *black cross* is a marker to locate the imaging region before and after straining

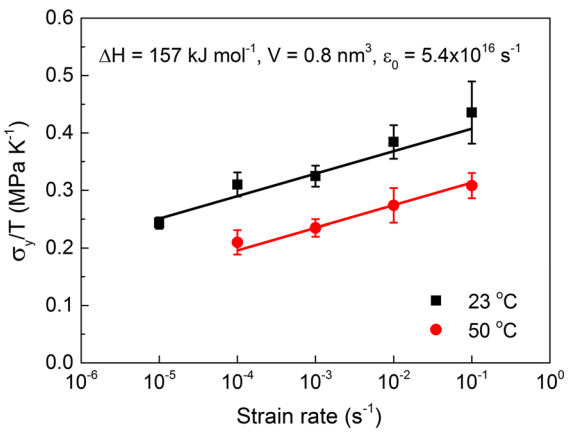

Fig. 8 Strain rate and temperature dependence of the normalized yield stress of cellulose nanopaper, indicating that the yield stress increases with increasing strain rate and decreasing temperature

inelasticity (Lim et al. 2003). The activation energy which is defined as the energy barrier for the molecular process is 157 kJ mol^{-1}. This value is much higher than the dissociation energy of hydrogen bonding which ranges from 20 to 50 kJ mol^{-1} (Bohidar 2015) but lower than the dissociation energy of C–C and C–O covalent bonds ranging from 300 to 500 kJ mol^{-1} (Blanksby and Ellison 2003; Chaléat et al. 2008), suggesting that hydrogen bonds were broken when cellulose nanopaper was loaded in the inelastic region. Therefore, this study suggests that the inelastic behaviour of cellulose nanopaper originates from molecular mobility in amorphous regions favoured by breakage of hydrogen bonds.

In order to study these molecular processes in more detail, possible relaxation processes in cellulose nanofibres were examined using dielectric spectroscopy. Figure 9 shows the temperature dependence of the dielectric loss at different frequencies. Two dielectric loss peaks can be identified at a frequency of 100 Hz. For polarized polymers, this dielectric loss is primarily from overcoming friction during changing of chain conformation under an alternating applied electric field. Therefore, a dielectric loss peak represents a state when the chain mobility does not match the alternation of the applied electric field. The dielectric properties of cellulose have been extensively investigated (Jafarpour et al. 2007; Rachocki et al. 2005; Roig et al. 2011). The peak of the dielectric loss at low temperature is usually assigned to

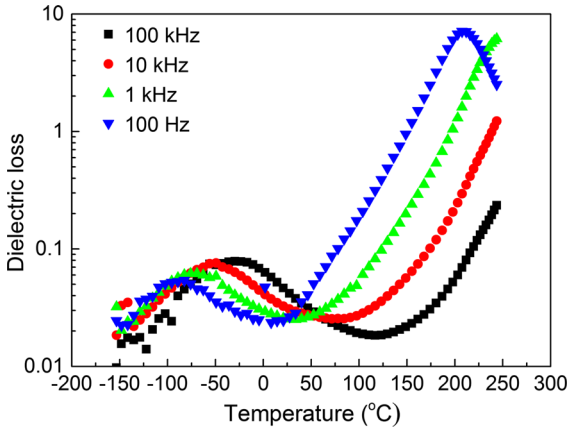

Fig. 9 Dielectric loss versus temperature at different frequencies for cellulose nanopaper, showing two dielectric loss peaks at different temperatures. The peaks move towards higher temperatures for higher frequencies

secondary relaxation while the one at higher temperature is attributed to primary relaxation or specifically the dielectric manifestation of the glass transition (Roig et al. 2011).

It is worth noting that dielectric loss peaks move to higher temperature for higher frequencies of applied electric field. This behaviour is consistent with the strain rate and temperature dependence of the yield stress. Since the strain rate and temperature dependence of the yield stress is associated with a single molecular process (motion in molecules in amorphous regions represented by yield stress as a linear function of strain rate in Fig. 8), one may assume that the inelastic behaviour of cellulose nanopaper is strongly associated with segmental motion of the molecular main chain.

Conclusions

Cellulose nanopaper is a strong and tough fibrous network composed of hydrogen bonded cellulose nanofibres. Upon loading, it shows significant inelastic behaviour which results in its high toughness. Strain mapping using 2D DIC revealed that inelasticity occurs all over the sample. Mechanical testing and Raman spectroscopy indicated that inelasticity is not the result of large scale reorientation of cellulose nanofibres in the network. 2D WAXD patterns suggested that also molecular reorientation in crystalline regions is not responsible for the inelastic behaviour. On the other hand, POM images revealed a transition from an isotropic amorphous structure to an anisotropic structure after straining. Eyring's theory was used to describe the strain rate and temperature dependence of the yield stress. This suggests that the inelastic behaviour is associated with a single molecular process, which is supported by the POM results which indicate that inelasticity takes place within the nanofibres. The activation energy of this process was sufficient to break the van der Waals or hydrogen bonds between the nanofibres or cellulose molecules but not enough to break the covalent bonds within the individual nanofibres. The temperature dependence of the dielectric loss showed that inelasticity occurred in a temperature range where primary relaxation dominates. In short, the current work hints that segment motion of molecules in amorphous regions is an important cause for the inelastic region in the stress–strain curve of cellulose nanopaper at a dry state. However, other toughening mechanisms such as fibre slippage and reorientation may become active and contribute to the inelastic mechanical behaviour of cellulose nanopaper at a wet state.

Acknowledgments The authors would like to thank Dr. Rory Wilson for the technical help in XRD. The authors would also like to acknowledge Prof. Lars Berglund from the Wallenberg Wood Science Center at the KTH Stockholm for providing cellulose nanofibres and stimulating discussions on toughening mechanisms. R.M. would like to acknowledge the China Scholarship Council (CSC) scheme for their financial support.

Compliance with ethical standards

Conflict of interest The authors declare that they have no conflict of interest.

References

Alcock B, Cabrera NO, Barkoula NM, Reynolds CT, Govaert LE, Peijs T (2007) The effect of temperature and strain rate on the mechanical properties of highly oriented polypropylene tapes and all-polypropylene composites. Compos Sci Technol 67:2061–2070. doi:10.1016/j.compscitech.2006.11.012

Arévalo R, Peijs T (2016) Binderless all-cellulose fibreboard from microfibrillated lignocellulosic natural fibres. Compos Part A Appl Sci Manuf 83:38–46. doi:10.1016/j.compositesa.2015.11.027

Barnett JR, Bonham VA (2004) Cellulose microfibril angle in the cell wall of wood fibres. Biol Rev 79:461–472. doi:10.1017/S1464793103006377

Benitez AJ, Torres-Rendon J, Poutanen M, Walther A (2013) Humidity and multiscale structure govern mechanical properties and deformation modes in films of native cellulose nanofibrils. Biomacromolecules 14:4497–4506. doi:10.1021/bm401451m

Bhupathi P, Jaworski L, Hwang J, Tanner DB, Obukhov S, Lee Y, Mulders N (2010) Optical birefringence in uniaxially compressed aerogels. New J Phys 12:103016. doi:10.1088/1367-2630/12/10/103016

Blaber J, Adair B, Antoniou A (2015) Ncorr: open-source 2D digital image correlation matlab software. Exp Mech 55:1105–1122. doi:10.1007/s11340-015-0009-1

Blanksby SJ, Ellison GB (2003) Bond dissociation energies of organic molecules. Acc Chem Res 36:255–263. doi:10.1021/ar020230d

Bohidar HB (2015) Fundamentals of polymer physics and molecular biophysics. Cambridge University Press, Cambridge

Born M, Wolf E (1999) Principles of optics. Cambridge University Press, Cambridge

Chaléat CM, Michel-Amadry G, Halley PJ, Truss RW (2008) Properties of a plasticised starch blend—part 2: influence of strain rate, temperature and moisture on the tensile yield behaviour. Carbohydr Polym 74:366–371. doi:10.1016/j.carbpol.2008.03.002

Eichhorn SJ, Sirichaisit J, Young RJ (2001a) Deformation mechanisms in cellulose fibres, paper and wood. J Mater Sci 36:3129–3135. doi:10.1023/A:1017969916020

Eichhorn SJ, Young RJ, Yeh WY (2001b) Deformation processes in regenerated cellulose fibers. Text Res J 71:121–129. doi:10.1177/004051750107100206

Eichhorn SJ, Dufresne A, Aranguren M et al (2010) Review: current international research into cellulose nanofibres and nanocomposites. J Mater Sci 45:1–33. doi:10.1007/s10853-009-3874-0

Engels TAP, Söntjens SHM, Smit TH, Govaert LE (2010) Time-dependent failure of amorphous polylactides in static loading conditions. J Mater Sci 21:89–97. doi:10.1007/s10856-009-3851-9

French AD (2014) Idealized powder diffraction patterns for cellulose polymorphs. Cellulose 21:885–896. doi:10.1007/s10570-013-0030-4

French AD, Cintrón MS (2013) Cellulose polymorphy, crystallite size, and the segal crystallinity index. Cellulose 20:583–588. doi:10.1007/s10570-012-9833-y

Fukuzumi H, Saito T, Isogai A (2013) Influence of TEMPO-oxidized cellulose nanofibril length on film properties. Carbohydr Polym 93:172–177. doi:10.1016/j.carbpol.2012.04.069

Gierlinger N, Schwanninger M, Reinecke A, Burgert I (2006) Molecular changes during tensile deformation of single wood fibers followed by Raman microscopy. Biomacromolecules 7:2077–2081. doi:10.1021/bm060236g

Govaert LE, Peijs T (1995) Influence of applied stress and temperature on the deformation behavior of high-strength poly(vinyl alcohol) fibres. Polymer 36:3589–3592. doi:10.1016/0032-3861(95)92032-A

Hagman A, Nygårds M (2012) Investigation of sample-size effects on in-plane tensile testing of paperboard. Nord Pulp Pap Res J 27:295–304. doi:10.3183/NPPRJ-2012-27-02-p295-304

Haslach HW (2000) The moisture and rate-dependent mechanical properties of paper: a review. Mech Time-Depend Mater 4:169–210. doi:10.1023/A:1009833415827

Henriksson M, Henriksson G, Berglund LA, Lindström T (2007) An environmentally friendly method for enzyme-assisted preparation of microfibrillated cellulose (MFC) nanofibers. Eur Polym J 43:3434–3441. doi:10.1016/j.eurpolymj.2007.05.038

Henriksson M, Berglund LA, Isaksson P, Lindström T, Nishino T (2008) Cellulose nanopaper structures of high toughness. Biomacromolecules 9:1579–1585. doi:10.1021/bm800038n

Hsieh YC, Yano H, Nogi M, Eichhorn SJ (2008) An estimation of the Young's modulus of bacterial cellulose filaments. Cellulose 15:507–513. doi:10.1007/s10570-008-9206-8

Jafarpour G, Dantras E, Boudet A, Lacabanne C (2007) Study of dielectric relaxations in cellulose by combined DDS and TSC. J Non-Cryst Solids 353:4108–4115. doi:10.1016/j.jnoncrysol.2007.06.026

Kanters MJW (2015) Prediction of long-term performance of load-bearing thermoplastics. Dissertation, Technische Universiteit Eindhoven

Kargarzadeh H, Ahmad I, Abdullah I, Dufresne A, Zainudin SY, Sheltami RM (2012) Effects of hydrolysis conditions on the morphology, crystallinity, and thermal stability of cellulose nanocrystals extracted from kenaf bast fibers. Cellulose 19:855–866. doi:10.1007/s10570-012-9684-6

Keckes J, Burgert I, Frühmann K et al (2003) Cell-wall recovery after irreversible deformation of wood. Nat Mater 2:810–813. doi:10.1038/nmat1019

Klemm D, Philipp B, Heinze T, Heinze U, Wagenknecht W (1998) Comprehensive cellulose chemistry. Wiley, Chichester

Lim JY, Donahue HJ, Kim SY (2003) Strain rate, temperature, and microstructure-dependent yield stress of poly (ethylene terephthalate). Macromol Chem Phys 204:653–660. doi:10.1002/macp.200390033

Mao R, Goutianos S, Tu W, Meng N, Chen S, Peijs T (2017) Modelling the elastic properties of cellulose nanopaper. Mater Des 126:183–189. doi:10.1016/j.matdes.2017.04.050

Mulliken AD, Boyce MC (2006) Mechanics of the rate-dependent elastic–plastic deformation of glassy polymers from low to high strain rates. Int J Solids Struct 43:1331–1356. doi:10.1016/j.ijsolstr.2005.04.016

Österberg M, Vartiainen J, Lucenius J, Hippi U, Seppälä J, Serimaa R, Laine J (2013) A fast method to produce strong NFC films as a platform for barrier and functional materials. ACS Appl Mater Interfaces 5:4640–4647. doi:10.1021/am401046x

Park S, Baker JO, Himmel ME, Parilla PA, Johnson DK (2010) Cellulose crystallinity index: measurement techniques and

their impact on interpreting cellulase performance. Biotechnol Biofuels 3:10. doi:10.1186/1754-6834-3-10

Quero F, Nogi M, Yano H, Abdulsalami K, Holmes SM, Sakakini BH, Eichhorn SJ (2010) Optimization of the mechanical performance of bacterial cellulose/poly(L-lactic) acid composites. ACS Appl Mater Interfaces 2:321–330. doi:10.1021/am900817f

Quero F, Nogi M, Lee KY, Poel GV, Bismarck A, Mantalaris A, Yano H, Eichhorn SJ (2011) Cross-linked bacterial cellulose networks using glyoxalization. ACS Appl Mater Interfaces 3:490–499. doi:10.1021/am101065p

Rachocki A, Markiewicz E, Tritt-Goc J (2005) Dielectric relaxation in cellulose and its derivatives. Acta Phys Pol A 108:137–145. doi:10.12693/APhysPolA.108.137

Roig F, Dantras E, Dandurand J, Lacabanne C (2011) Influence of hydrogen bonds on glass transition and dielectric relaxations of cellulose. J Phys D Appl Phys 44:045403. doi:10.1088/0022-3727/44/4/045403

Salmén NL (1986) The cell wall as a composite structure. In: Bristow JA, Kolseth P (eds) Paper: structure and properties. Marcel Dekker, New York, pp 51–73

Segal L, Creely JJ, Martin AE, Conrad CM (1959) An empirical method for estimating the degree of crystallinity of native cellulose using the X-ray diffractometer. Text Res J 29:786–794. doi:10.1177/004051755902901003

Sehaqui H, Zhou Q, Ikkala O, Berglund LA (2011) Strong and tough cellulose nanopaper with high specific surface area and porosity. Biomacromolecules 12:3638–3644. doi:10.1021/bm2008907

Sehaqui H, Mushi NE, Morimune S, Salajkova M, Nishino T, Berglund LA (2012) Cellulose nanofiber orientation in nanopaper and nanocomposites by cold drawing. ACS Appl Mater Interfaces 4:1043–1049. doi:10.1021/am2016766

Senden DJA, van Dommelen JAW, Govaert LE (2012) Physical aging and deformation kinetics of polycarbonate. J Polym Sci Part B Polym Phys 50:1589–1596. doi:10.1002/polb.23161

Söntjens SHM, Engels TAP, Smit TH, Govaert LE (2012) Time-dependent failure of amorphous poly-D,L-lactide: influence of molecular weight. J Mech Behav Biomed Mater 13:69–77. doi:10.1016/j.jmbbm.2012.04.014

Tanpichai S, Quero F, Nogi M et al (2012) Effective Young's modulus of bacterial and microfibrillated cellulose fibrils in fibrous networks. Biomacromolecules 13:1340–1349. doi:10.1021/bm300042t

Tingaut P, Zimmermann T, Lopez-Suevos F (2010) Synthesis and characterization of bionanocomposites with tunable properties from poly(lactic acid) and acetylated microfibrillated cellulose. Biomacromolecules 11:454–464. doi:10.1021/bm901186u

Van Erp TB, Reynolds CT, Peijs T, Van Dommelen JAW, Govaert LE (2009) Prediction of yield and long-term failure of oriented polypropylene: kinetics and anisotropy. J Polym Sci Pol Phys 47:2026–2035. doi:10.1002/polb.21801

Wiley JH, Atalla RH (1987) Band assignments in the Raman spectra of celluloses. Carbohydr Res 160:113–129. doi:10.1016/0008-6215(87)80306-3

Zhu H, Zhu S, Jia Z et al (2015) Anomalous scaling law of strength and toughness of cellulose nanopaper. Proc Natl Acad Sci USA 112:8971–8976. doi:10.1073/pnas.1502870112